Mid-infrared plasmon-enhanced spectroscopy with germanium antennas on silicon substrates

Journal:	*Nano Letters*
Manuscript ID	nl-2015-03247s.R1
Manuscript Type:	Communication
Date Submitted by the Author:	08-Oct-2015

Complete List of Authors:	Baldassarre, Leonetta; Università di Roma La Sapienza; Istituto Italiano di Tecnologia Sakat, Emilie; Politecnico di Milano, Frigerio, Jacopo; Politecnico di Milano, Samarelli, Antonio; University of Glasgow, Gallacher, Kevin; University of Glasgow, Calandrini, Eugenio; Università di Roma La Sapienza, Isella, Giovanni; Politecnico di Milano, Paul, Douglas; University of Glasgow, Ortolani, Michele; Sapienza University of Rome, Physics Dept. Biagioni, Paolo; Politecnico di Milano, Physics

Mid-infrared plasmon-enhanced spectroscopy with germanium antennas on silicon substrates

Leonetta Baldassarre[1,2,‡], Emilie Sakat[3,‡], Jacopo Frigerio[4], Antonio Samarelli[5], Kevin Gallacher[5], Eugenio Calandrini[1], Giovanni Isella[4], Douglas J. Paul[5], Michele Ortolani[1], Paolo Biagioni[3,]*

[1]Dipartimento di Fisica, Università di Roma "La Sapienza", Piazzale Aldo Moro 5, I-00185 Roma, IT

[2]Center for Life Nano Science@Sapienza, Istituto Italiano di Tecnologia, Viale Regina Elena 291, I-00161 Roma, IT

[3]Dipartimento di Fisica, Politecnico di Milano, Piazza Leonardo da Vinci 32, I-20133 Milano, IT

[4]LNESS, Dipartimento di Fisica del Politecnico di Milano, polo di Como, via Anzani 42, I-22100 Como, IT

[5]School of Engineering, University of Glasgow, Rankine Building, Oakfield Avenue, Glasgow G12 8LT, UK

ABSTRACT

Mid-infrared plasmonic sensing allows the direct targeting of unique vibrational fingerprints of molecules. While gold has been used almost exclusively so far, recent research has focused on semiconductors with the potential to revolutionize plasmonic devices. We fabricate antennas out of heavily-doped Ge films epitaxially grown on Si wafers and demonstrate up to two orders of magnitude signal enhancement for the molecules located in the antenna hot spots compared to those located on a bare silicon substrate. Our results set a new path towards integration of plasmonic sensors with the ubiquitous CMOS platform.

KEYWORDS Silicon Technology, Plasmonics, Mid-Infrared Spectroscopy, Explosives Detection

TEXT

Localized plasmon resonances are nowadays recognized as one of the most powerful mechanisms to boost the interaction between light and matter at the nanoscale. In this frame, recent plasmonic research has searched for novel material platforms which can improve the quality and integrability of plasmonic interfaces and devices [1]. The choice of the material can impact on the crystalline and nanofabrication quality of the device, the spectral range of operation, and the amount of loss. The crucial issue for the future use of plasmonics in everyday applications, however, is the integration with the Si-complementary metal-oxide semiconductor (CMOS) technology process. This is difficult to foresee using the most common metal in plasmonics, gold, due to it being a deep level impurity and a fast diffuser which is incompatible with silicon technology. Among all applications of plasmonics, molecular sensing has already made its way to the market. Plasmonic sensors can be based on refractive index variations at the metal surface [2, 3], on the local enhancement of the electric field for Raman spectroscopy [4, 5], or on the modification of the engineered transmitted or reflected wavefront in antennas by a resonant molecular vibration in the mid-infrared (IR) [4, 6-16]. In the last few years the latter approach, mainly pursued with the nanofabrication of gold antennas, led to reported signal enhancements exceeding three orders of magnitude for the material located in the antenna hot spots compared to the material outside the hotspots.

While metals are the most natural choice for visible and near-IR plasmonics, it has been suggested that heavily-doped semiconductors (i.e. degenerately-doped to be metallic) could replace and, possibly, outperform metals in the mid-IR frequency range [1, 14-25]. The envisioned advantages for plasmonic device design include (i) the low absolute values of the dielectric constant in the mid-IR, strictly resembling that of metals in the visible and near-IR

range but without the detrimental effect of interband transition losses, (ii) the high material quality, thanks to single-crystalline epitaxial growth, (iii) in the case of foundry-compatible group-IV semiconductors like Si and Ge, the potential for on-chip integration of antennas, detectors and readout electronics, all fabricated in a single cost-effective silicon foundry manufacturing process, and (iv) the possibility of active electrical and/or optical tuning of the plasmonic effects by the control of the doping level. The onset of the plasmonic behavior of a conducting material is marked by the so-called plasma frequency ω_p, i.e. the frequency below which the real part of the dielectric constant of the material becomes negative. Standard doping of semiconductors usually sets ω_p in the far-IR, while entering the mid-IR range requires high doping levels, n up to 10^{19}-10^{20} cm^{-3} according to the scaling law $\omega_p \propto \sqrt{\frac{n}{m_e}}$, m_e being the electron effective mass.

In particular, the development of a plasmonic platform for molecular sensing based on group-IV semiconductors [20-25] could have a dramatic impact on chemical or biological laboratory applications because it could lead to the automation of surface-enhanced IR absorption spectroscopy (SEIRA) [26] by exploiting readily and massively available disposable substrates with integrated readout produced by standard silicon foundry processes. In the long term, semiconductor plasmonic integration could lead to low-cost, compact and efficient lab-on-a-chip devices for in-situ medical diagnostics, environmental monitoring in addition to safety and security sensing. Also, whilst the performance of semiconductor plasmonic antennas may not be the highest among all possible materials due to unavoidable losses in heavily doped materials, the ability to integrate readout electronics and reference standards close to the detectors may be

key to optimize the sensitivity, specificity and speed of the full sensor system, as has already been demonstrated e.g. in the development of CMOS single photon detector arrays [27].

In the last decade epitaxial Ge on Si has become a key technology for silicon photonics due to its demonstrated compatibility with the CMOS technology [28-30]. Band engineering and doping have already allowed for the demonstration of high-performance Ge photodiodes [31], optical modulators [32, 33], prototype near-IR and far-IR LEDs and laser diodes [34-36], and integrated systems [37]. Intrinsic Ge is also considered one of the best candidates for dielectric waveguides in the mid-IR range of interest for molecular sensing (wavelengths λ~20 to 4 μm, or frequency ω~500 to 2500 cm^{-1}) [38, 39]. The preference of Ge over Si is due to negligible absorption losses compared to Si [30], which instead features relatively strong IR-active transitions in the 400-1700 cm^{-1} range related to the presence of in-gap defect states. Such Si dipole-active impurity states result in a large number of narrow absorption lines that may overlap to the weak molecular signals of surface-enhanced sensors and complicate their interpretation [40]. Ge, on the other side, displays no impurity absorption lines in the 100-2000 cm^{-1} range and therefore it is commonly employed for thick mid-IR optical elements such as lenses and prisms. For applications in mid-IR plasmonics, in particular, Ge has been rarely if at all been used despite the appealing perspective of combining infrared spectroscopy with CMOS integration. When compared with Si, it has the advantage of a smaller electron effective mass ($m_e \approx 0.12$ for n-type Ge and $m_e \approx 0.26$ for n-type Si), which widens the range of applications of plasmonic sensing (allowing for higher ω_p) for a given doping level. This is especially relevant because of the technological issues in achieving extremely high doping levels and because plasmonic losses in doped semiconductors are also influenced by free-carrier scattering by charged impurities, thereby favoring materials that can achieve higher plasma frequencies for a given doping level.

In this work we grow epitaxial Ge films on standard Si wafers using the low-energy plasma-enhanced chemical vapor deposition (LEPECVD, see Supporting Information, Section A) method [41, 42] and exploit phosphorus as the donor to achieve a doping level $n \approx 2.3 \cdot 10^{19}$ cm^{-3}, thus setting $\omega_p \approx 1000$ cm^{-1} (≈ 10 μm wavelength). Micrometer-sized antennas are fabricated out of the epitaxial Ge material by electron-beam lithography and reactive ion etching processes and are characterized by Fourier-transform IR (FTIR) spectroscopy demonstrating localized plasmon resonances in the 400 - 900 cm^{-1} range. Finally, the fabricated devices are used for plasmon-enhanced sensing experiments, detecting the vibrational fingerprints of thin molecular films and liquids and demonstrating signal enhancements of up to two orders of magnitude when the target materials are located at the antenna hotspots.

In order to design the antenna samples, we employ frequency- and time-domain simulations (see Supporting Information, Section A). The dielectric constant of the Ge material for simulations is obtained by numerical fitting of the reflection and transmission FTIR data obtained from unpatterned Ge films in the entire infrared range (see Supporting Information, Section B). The investigated antenna designs, demonstrated in Fig. 1, have fixed thickness and width of the order of 1 μm (i.e. comparable with the skin depth of the doped Ge in the 400 - 900 cm^{-1} range) and a range of arm lengths L varying from 1 to 4 μm (see Supporting Information, Section C). We considered both single-arm (gapless) and double-arm (gap) antennas. The simulations reveal the existence of two longitudinal antenna resonances related to two distinct plasmonic modes propagating along the antenna arms. The first mode ('substrate-like', labelled as R1) lies in the 300-500 cm^{-1} range with the hotspots located at the Si/Ge interface, while the second mode ('air-like', R2) lies in the 800 - 900 cm^{-1} range with hotspots at the upper antenna edges towards the air half-space. Field intensity maps of the two modes at

their respective near-field resonance frequencies are presented in Fig. 1. It should be stressed here that a slight spectral shift occurs between the near-field and far-field resonances of the investigated antennas (see Supporting Information, Section C), which is common for lossy plasmonic materials [43]. The electromagnetic origin of the two modes is the same in single-arm and double-arm antennas. The presence of the gap, however, affects the local intensity distribution, further boosting the enhancement and confinement of the field. The evidence for these two modes has already been reported in the literature [17-19]. In particular, the air-like R2 mode is the most promising mode for sensing applications because (i) the fields are located towards the air half-space and therefore interact more effectively with the molecules to be detected and (ii) the higher frequency compared to R1 is an advantage in view of the inherent difficulty in growing high-quality semiconductor materials with heavy doping and therefore with high plasma frequency.

A representative scanning electron microscopy (SEM) image of a fabricated gap antenna sample is presented in Fig. 2a. The gap between the two arms is 300 nm, while the period for the array is large enough to avoid significant near-field interactions between neighboring antennas. The samples are characterized by FTIR spectroscopy, measuring both the transmission and reflection spectra at normal incidence with the electric field linearly polarized along the antenna axis as sketched in Fig. 2b. In the perspective of an integrated CMOS sensing device, however, it is worth discussing the antenna signatures in reflection geometry. Indeed the use of an optical scheme based on reflection instead of transmission is key in developing realistic mid-IR chemical sensing devices as it can be coupled to e.g. a sensing chip equipped with microfluidics (aqueous solutions are not transparent at mid-IR frequencies) [6]. Additionally, the measured

transmission suffers from light diffusion coming from the backside roughness [17] and from absorptions in a thick Si substrate with a standard concentration of impurities [30].

Fig. 2b-d demonstrates a comparison between the calculated and measured reflection and extinction spectra of three different antennas, namely two single-arm antennas with lengths L = 2.0 μm and 3.0 μm, respectively, and one gap antenna with L = 2.0 μm for the individual antenna arms. In order to extract the antenna response, we demonstrate in Fig. 2b-d a normalized extinction $E_{\mathrm{norm}} = 1 - \frac{T_{\mathrm{ant}}}{T_{\mathrm{Si}}}$, with T_{ant} and T_{Si} being the transmission spectra acquired from the antenna sample and from the bare Si substrate, respectively, and the reflection $R = \frac{R_{\mathrm{ant}}}{R_{\mathrm{Au}}}$, with R_{ant} and R_{Au} being the reflection spectra acquired from the antenna sample and from a bare Au mirror, respectively. The experimental results (solid lines in the left column) clearly display two resonances corresponding to the R1 and R2 modes described before. Noticeably, the two spectral features are not present in geometrically identical antennas fabricated out of lightly doped Ge on Si ($n \approx 1.5 \cdot 10^{17}$ cm^{-3} and $\omega_p < 100$ cm^{-1}, dashed lines), which acts as a purely dielectric material in the investigated frequency range, thus demonstrating that the resonances observed in the doped samples are due to localized plasmons of the conduction electrons. This is also in agreement with the redshift of the resonances with increasing arm length (compare the spectra of 2- and 3-μm single-arm antennas in Figs. 2b and 2d), as expected for plasmonic antennas [44]. We have also verified that the two strong resonant features disappear when the excitation electric field is oriented perpendicular to the antenna axis and only the much weaker transverse resonances are excited (see Supporting Information, Section E).

The simulated spectra at normal incidence for the investigated antenna samples, also displayed in Fig. 2b-d, are in excellent agreement with the experiments, with small discrepancies that can

be attributed mainly to uncertainties in the value of the dielectric constant. Calculations have also been performed to confirm that no collective behavior contributes to the R1 and R2 resonance mechanisms. The spectral positions of the resonances have been found to be largely independent of the incidence angle of excitation and periodicity of the array (see Supporting Information, Section C and E), which highlights the localized character of the two resonances and confirms that we are indeed addressing the plasmonic response of individual antennas. This paves the way towards engineered devices where individual semiconductor antennas, each one with a specific spectral response, are integrated on the same miniaturized silicon chip. Only in the case of Fig. 2d, the reader should notice that the asymmetric shape of the peak around 400 cm^{-1} is due to the occurrence of a Rayleigh anomaly, as thoroughly discussed in the Supporting Information (Section C).

With this understanding of the plasmonic properties of the antenna samples, we have explored the potential for sensing using a reflection geometry, which is best suited for on-chip integrated antennas. We have exploited the R2 resonance for the sensing of both thin solid-state layers and liquid-phase droplets of substances with vibrational fingerprints in the spectral window covered by R2.

In a first experiment (see Fig. 3), we have coated the same antennas of Fig. 2 with a polydimethylsiloxane (PDMS) layer, which features a vibrational absorption resonance at 800 cm^{-1} (see Supporting Information, Section F) due to the Si-C bond stretching modes. This absorption line matches very well the spectral position of the R2 near-field resonance of the antennas, as demonstrated in Fig. S4 of the Supporting Information. By spin-coating the highly diluted PDMS and further curing, we obtained a PDMS thickness below 40 nm, as demonstrated in the SEM cross-section images of the PDMS-coated Ge antennas (obtained by the slice-and-

view technique with a dual electron and ion beam apparatus) in Fig. 3a. Reflection spectra for the antenna samples are displayed in Fig. 3b. A comparison between the reflection spectra of the clean samples (dashed lines) and of the spin-coated samples (solid lines), reveal that the PDMS layer induces two changes in the spectra: a slight redshift of the plasmonic resonance, due to the increased refractive index in the antenna surroundings, and the appearance of an asymmetric spectral line around 800 cm^{-1}. Such Fano-like interferences have already been the subject of extensive studies in the literature [7, 12, 45-47]. In order to provide further support to the actual interaction between the PDMS vibrational resonances and the plasmonic field of the antennas, we also acquired reflection spectra after covering the antennas with a polymer (AZ-5214) having similar refractive index to PDMS but very weak absorption features in the spectral window under consideration (see also Section G of the Supporting Information). In this way, we obtained correctly red-shifted reference antenna spectra that can be used for background subtraction from those obtained from PDMS-covered antennas. Through this experiment, we are able to demonstrate (see Fig. 3c) that the line-shape around 800 cm^{-1} is completely different for parallel and perpendicular polarization and that the line-shape obtained for perpendicular polarization is similar to the one obtained from nominally undoped antenna samples. This observation clearly highlights the electromagnetic coupling between PDMS and the longitudinal plasmon resonances.

We also calculated (see Section H of the Supporting Information) the ratio between the experimental spectra acquired from PDMS-coated antennas with parallel and perpendicular polarization, both for the doped and undoped samples. Noticeably, the 800 cm^{-1} vibrational feature from PDMS completely disappears in the undoped antennas after such normalization, meaning that no PDMS-antenna interaction is taking place irrespective of the field polarization.

On the other side, a clear Fano-like line survives when the same normalization is performed for doped antenna samples, again unambiguously highlighting the role of longitudinal localized plasmon resonances.

We now focus our attention on the gap antennas, which display the strongest field enhancement. Fig. 4a (left panel) provides a comparison between the spectra acquired with the polarization parallel (solid line) and perpendicular (dashed line) to the antenna axis. The experimental results compare well with those from numerical simulations, also presented in Fig. 4a (right panel). It should be noted here that, as observed in the SEM image in Fig. 3a, the PDMS does not conformally cover the antenna gap, rather a PDMS meniscus is created due to the surface tension. This is fully taken into account in the simulations. Clearly, since the hotspots related to the R2 resonance are located right at the upper antenna edges, where the PDMS adheres almost perfectly to the antenna, this does not compromise the sensing experiment. The use of an antenna resonance with the associated field hotspots located in the air half space is therefore confirmed to be an interesting feature that simplifies the requirements for analyte delivery into the antenna gap.

In order to further clarify the role of the plasmonic hotspots, we also ran two separate simulations (see Fig. 4b), a first one with PDMS placed only in the hotspots (black lines in Fig. 4c) and a second one with the PDMS coating everywhere except in the hotspots (red lines in Fig. 4c). The total PDMS volume in the former simulation is about 100 times smaller than in the latter. In the left panel of Fig. 4c, for the perpendicular field polarization and PDMS only in the hotspots, the simulations do not display any detectable sign of the PDMS vibrational mode at 800 cm^{-1}. On the contrary, when the PDMS coating is everywhere except in the hotspots the vibrational mode is clearly visible. This behavior is at complete variance with what observed in

the right panel of Fig. 4c, i.e. for electric field polarization parallel to the antenna axis. Therein, one clearly observes that the PDMS absorption line is visible in both simulations (PDMS only in the hot spots and PDMS everywhere else). Indeed, while having a different line-shape because of the interaction with the plasmonic resonance when the PDMS is in the hotspots, the two vibrational features have roughly the same spectral weight, indicating that the respective perturbations to the antenna spectrum have similar strengths. Since the simulated PDMS volume in the hotspots only is about 100 times smaller than outside the hotspots, we estimate an enhancement factor of up to two orders of magnitude for the optical signal generated by the PDMS in the hotspots, compared to the PDMS outside the hotspots.

It is important here to stress that the experimentally observed line shape (Fig. 4a, left panel) is interpreted as the far-field interference of the two contributions outlined in Fig. 4c for the parallel polarization (black and red lines in the right panel). Their individual line shapes are determined by two mechanisms: on the one side, the reflection geometry is known to produce Fano-like features because of the interference between the light interacting with the PDMS layer and that directly reflected by the substrate [46]. On the other side, we have the interaction between the PDMS and the antenna resonance in the hot spots. The situation is further complicated by the presence of shoulders and side peaks in the PDMS vibrational feature around 800 cm-1 (see Section F of the Supporting Information). The overall interference process between the two contributions in Fig. 4c, each one carrying its own specific phase, is therefore not easy to deconvolve, yet it is accurately described and predicted by full-wave simulations in Fig. 4a (right panel). Incidentally, one may notice that the estimated two-order-of-magnitude enhancement in the sensing experiment is slightly larger than the average local intensity enhancement expected in the antenna hot spots (see Fig. 1). This must likely be ascribed to small uncertainties in the

dielectric description of the Ge/PDMS system and in the evaluation of the enhancement for the sensing experiment. , an intriguing possibility is also that the sensing enhancement might be proportional to the square of the local intensity enhancement, as already pointed out in Ref. 48, since the antenna works both as a receiving and as an emitting transducer for the electromagnetic radiation.

Finally, we applied Ge plasmonic antennas to the sensing of chloroethyl methyl sulfide (CEMS), a transparent liquid with mass density similar to that of water that is a simulant of common explosive materials and cannot easily be distinguished from harmless liquids, except by spectroscopy. During the experiment (Fig. 5a), the decrease in thickness of the droplet due to evaporation was monitored with the same spectroscopy setup used for the sensing demonstration by continuously acquiring fast FTIR spectra every 5 seconds and by measuring the period of the Fabry-Pérot interference fringes in the near-IR. When the droplet thickness was estimated to be below 2 μm, longer FTIR spectra with higher signal-to-noise ratio were acquired. Due to the large volatility of the investigated substances, we are not able to quantitatively assess the exact fraction of liquid inside and outside the hotspots, so to provide a precise value of the signal enhancement due to the antennas. Fig. 5b demonstrates the IR absorption fingerprint spectrum of the pure substance (grey line), obtained in transmission geometry with a 20-μm-thick IR cuvette. A strong vibrational doublet appears at 690-720 cm^{-1}, i.e. below the plasma frequency of our material in the region of plasmonic behavior, while a second fingerprint of similar vibrational absorption strength appears around 1430 cm^{-1} in the region of dielectric behavior of the Ge, i.e. above the plasma frequency. In Fig. 5c we also demonstrate the spectrum of the doped Ge antennas covered with a droplet of CEMS (red line) superimposed onto the spectrum of the clean antenna sample (black dashed line). By taking the difference between these two spectra, the

vibrational molecular fingerprint of CEMS is clearly recovered (Fig. 5d). One can notice, however, that the relative spectral weight of the doublet at 690-720 cm^{-1} compared to the feature at 1430 cm^{-1} in Fig. 5d is stronger than in the bare liquid material of Fig. 5b, thus qualitatively pointing towards a signal enhancement provided by the plasmonic antenna response below the plasma frequency of our material (see also Supporting Information, Section J).

In conclusion, we have introduced a novel all-group-IV semiconductor material platform for mid-IR plasmonics, based on heavily doped Ge epitaxially grown on standard Si wafers. We demonstrated localized plasmon resonances in Ge antennas and exploited the fabricated devices for sensing experiments based on the resonant detection of molecular vibrational fingerprints of both condensed-phase and liquid-phase analytes. While the present work demonstrates doping levels of about $2.3 \cdot 10^{19}$ cm^{-3}, reaching a plasma frequency around 1000 cm^{-1}, the whole relevant fingerprint region extending roughly up to 1800 cm^{-1} can be in principle reached given the high solubility of P dopants in Ge [49] and the recent efforts to demonstrate carrier densities of the order of 10^{20} cm^{-3} in n-type Ge [50]. Enhancement factors of up to two orders of magnitude for the material located in the antenna hotspots have been obtained in the present work. Although the demonstrated enhancement is still below that obtained with state-of-the-art Au antennas [8,13] and the accessible wavelength range is slightly narrower than what has been obtained with III-V compound semiconductor antennas [17], the demonstrated Ge antennas are compatible with the silicon CMOS technology, which can in turn be used to build intelligent sensor networks with a very large number of sensing elements at a far lower cost. As in most direct CMOS applications, the performance of the single sensor must be traded for the number of identical sensors with integrated readout electronics that can be realized, when compared with optimized stand-alone antennas. The developed technology holds great promise for the realization of CMOS-

compatible mid-IR devices for substance-specific molecular sensing. The field enhancement in the plasmonic hotspots may also find applications in other fields where the on-chip integration of plasmonics with electronics is expected to play a key role, e.g. in IR imaging, light detection, and energy harvesting.

FIGURES

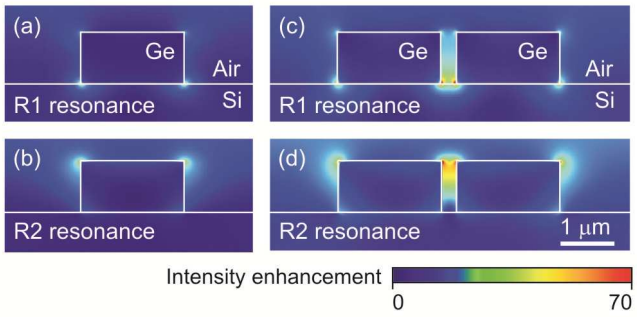

Figure 1. The field intensity distribution (squared modulus of the electric field) in the resonant Ge antennas: the simulated near-field intensity enhancement associated with the excitation of the localized plasmon modes labelled as R1 and R2 in the single-arm gapless antennas (a-b) and the double-arm gap antennas (c-d). All maps are calculated at the respective near-field resonance frequency. Each antenna arm is 2-μm long and the gap is 300 nm.

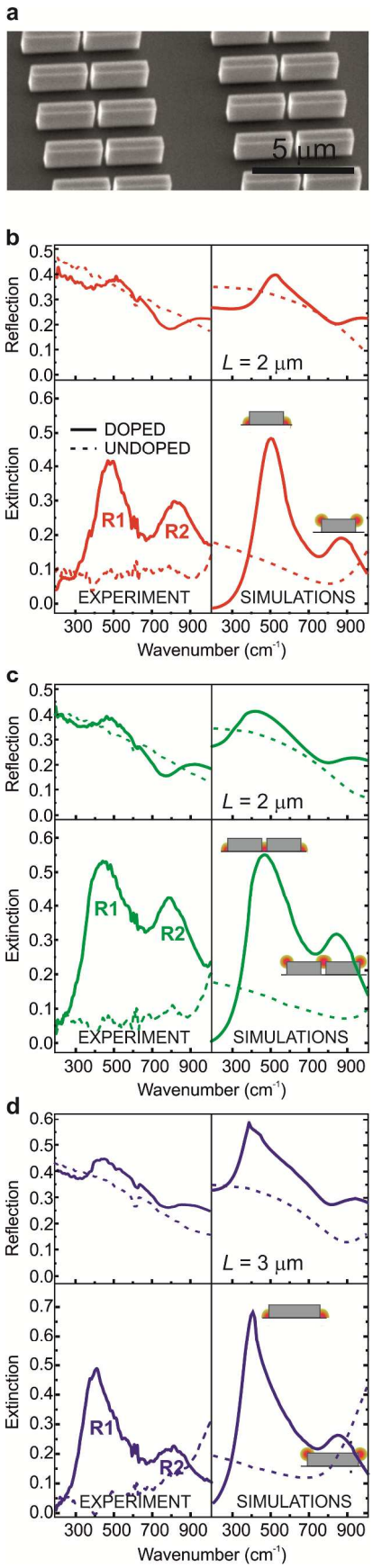
a
5 μm
b
Reflection
L = 2 μm
Extinction
DOPED
UNDOPED
R1
R2
EXPERIMENT
SIMULATIONS
Wavenumber (cm-1)
c
Reflection
L = 2 μm
Extinction
R1
R2
EXPERIMENT
SIMULATIONS
Wavenumber (cm-1)
d
Reflection
L = 3 μm
Extinction
R1
R2
EXPERIMENT
SIMULATIONS
Wavenumber (cm-1)

Figure 2. A demonstration of mid-IR plasmon resonances in Ge antennas: (a) a representative SEM image of a Ge antenna sample. (b)-(d) The experimental and simulated reflection and extinction spectra for single-arm antennas with L = 2.0 μm length (b), gap antennas with L = 2.0 μm arm length (c), and single-arm antennas with L = 3.0 μm length (d). The solid lines refer to doped plasmonic antennas and the dashed lines refer to undoped non-plasmonic antennas. For the sake of clarity, all the transmission spectra from the undoped antennas have been rescaled by 0.8 before the calculation of the normalized extinction ratio.

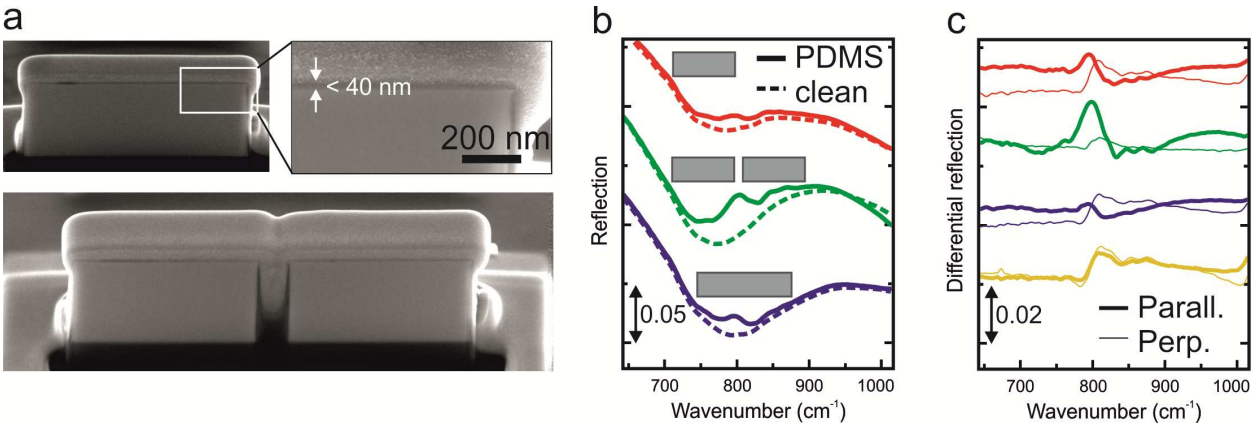

Figure 3. The solid-state sensing of a thin PDMS layer: (a) cross-sectional SEM images of the PDMS-covered antennas, obtained after deposition of a Pt overlayer with the slice-and-view technique in a dual-beam apparatus. The length of the single-arm antenna is 3 μm, while individual arms of the gap antenna are 2 μm long. (b) The experimental reflection spectra acquired after PDMS spin coating on the three antenna samples (solid lines) and reference spectra from the clean samples (dashed lines); the spectra have been translated vertically for the sake of clarity. (c) The difference spectra obtained after subtraction of the spectra from antennas coated with AZ-5214; the spectra have been translated vertically for the sake of clarity. Thicker lines correspond to polarization parallel to the antenna axis, thinner lines to perpendicular polarization. The color coding is the same as in panel b and the yellow lines refer to an undoped antenna sample.

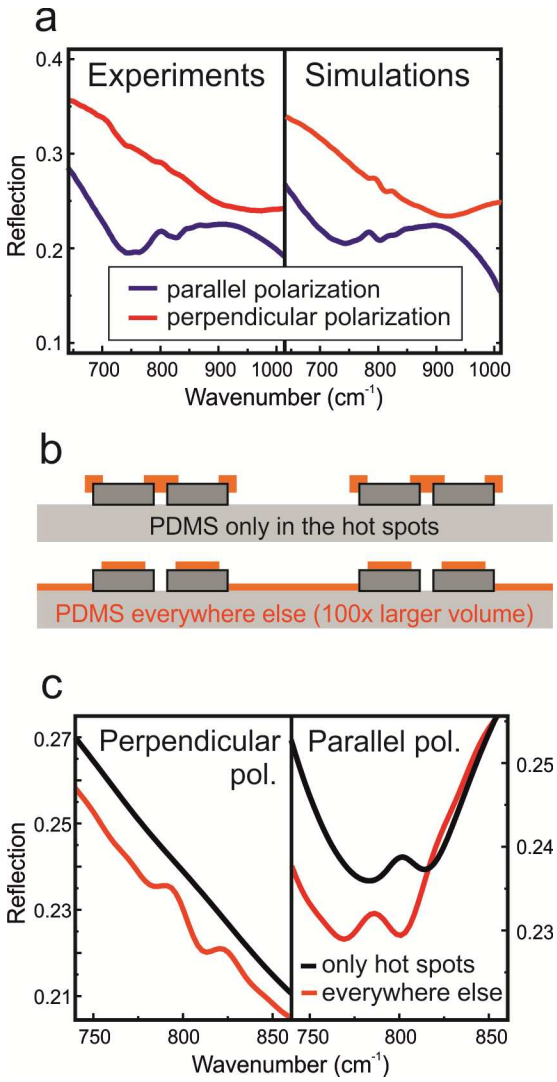

Figure 4. (a) The experimental (left panel) and simulated (right panel) reflection spectra from the PDMS-covered gap antenna sample, obtained with the field polarization parallel (blue line) or perpendicular (red line) to the antenna axis. The simulated spectra have been translated vertically for the sake of clarity. (b) Sketch of the PDMS distribution in the simulations demonstrated in panel c. (c) Simulations of reflection spectra highlighting the individual contributions coming from the antenna hot spots (black lines) and from everywhere else (red lines), for light with the polarization perpendicular to the antenna axis (left panel) and parallel to the antenna axis (right panel).

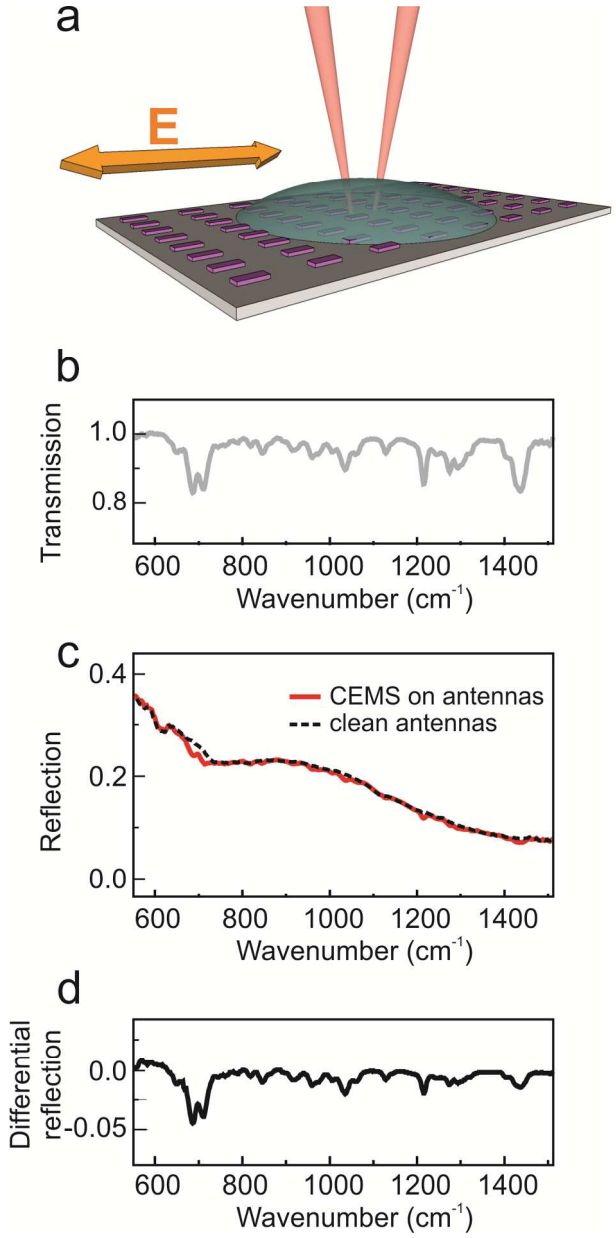

Figure 5. A hazardous liquid sensing experiment: (a) a sketch of the reflection sensing geometry; (b) the transmission spectrum of pure CEMS in a 20-μm-thick standard IR cuvette; (c) the reflection spectrum for a CEMS-covered antenna array (red line) and the reflection spectrum from the clean antenna array (black dashed line), and (d) the difference between the two spectra in panel c.

ASSOCIATED CONTENT

Supporting Information. Methods; dielectric constant extraction of the unpatterned Ge material; electromagnetic simulations; geometrical details of the samples investigated in the main manuscript; detailed analysis of the infrared spectra of the antenna arrays; absorbance spectra of PDMS and CEMS; PDMS sensing: comparison with a weakly-absirbing polymer; PDMS sensing: comparison with undoped antennas; PDMS sensing: role of the R1 resonance; CEMS sensing: simulated near-field enhancement. This material is available free of charge via the Internet at http://pubs.acs.org.

AUTHOR INFORMATION

Corresponding Author

*To whom correspondence should be addressed: paolo.biagioni@polimi.it

Author Contributions

‡These authors contributed equally. J.F. and G.I. performed the growth of heavily-doped Ge on Si. E.S. and P.B. performed the numerical simulations. A.S., K.G., and D.J.P. fabricated the devices. L.B., E.C., and M.O. performed the FTIR characterization. P.B., M.O., and D.J.P. coordinated the work and wrote the draft of the manuscript. All authors contributed extensively to the analysis and discussion of the results and to the revision of the manuscript.

Notes

The authors declare no competing financial interest.

Funding Sources

The research leading to these results has received funding from the European Union's Seventh Framework Programme under grant agreement n°613055.

ACKNOWLEDGMENT

The authors would like to thank the staff of the James Watt Nanofabrication Centre for help in fabricating the samples and A. De Ninno and A. Notargiacomo of CNR-IFN-Rome for the PDMS film preparation and inspection by focused ion beam. Fruitful discussions with M. Bollani, D. Brida, M. Celebrano, S. Collin, L. Duò, M. Finazzi, and P. Ghenuche are gratefully acknowledged.

REFERENCES

[1] Boltasseva A.; Atwater, H. A. *Science* **2011**, 331, 290-291.

[2] Liu, N.; Tang, M. L.; Hentschel, M.; Giessen, H.; Alivisatos, A. P. *Nature Mater.* **2011**, 10, 631-636.

[3] Svedendahl, M.; Chen, S.; Dmitriev, A.; Käll, M. *Nano Lett*. **2009**, 9, 4428-4433.

[4] D'Andrea, C.; Bochterle, J.; Toma, A.; Huck, Ch.; Neubrech, F.; Messina, E.; Fazio, B.; Maragò, O. M.; Di Fabrizio, E.; de La Chapelle, M. L.; Gucciardi, P. G.; Pucci, A. *ACS Nano*, **2013**, 7, 3522-3531.

[5] De Angelis, F.; Das, G.; Candeloro, P.; Patrini, M.; Galli, M.; Bek, A.; Lazzarino, M.; Maksymov, I.; Liberale, C.; Andreani, L. C.; Di Fabrizio, E. *Nature Nanotech.* **2010**, 5, 67-72.

[6] Adato, R.; Altug, H. *Nature Comm.* **2013**, 4, 2154-2163.

[7] Adato, R.; Artar, A.; Erramilli, S.; Altug, H. *Nano Lett.* **2013**, 13, 2584-2591.

[8] Adato, R.; Yanik, A. A.; Amsden, J. J.; Kaplan, D. L.; Omenetto, F. G.; Hong, M. K.; Erramilli, S.; Altug, H. *Proc. Natl. Acad. Sci.* **2009**, 106, 19227-19232.

[9] Brown, L. V.; Zhao, K.; King, N.; Sobhani, H.; Nordlander, P.; Halas, N. J. *J. Am. Chem. Soc.* **2013**, 135, 3688-3695.

[10] Limaj, O.; Lupi, S.; Mattioli, F.; Leoni, R.; Ortolani, M. *Appl. Phys. Lett.* **2011**, 98, 091902.

[11] Neubrech F.; Pucci, A.; Cornelius, Th. W.; Karim, S.; García-Etxarri, A.; Aizpurua, J. *Phys. Rev. Lett.* **2008**, 101, 157403.

[12] Wu, C.; Khanikaev, A. B.; Adato, R.; Arju, N.; Yanik, A. A.; Altug, H.; Shvets, G. *Nature Mater.* **2012**, 11, 69-75.

[13] Brown, L.V.; Yang, X.; Zhao, K.; Zheng, B.Y.; Nordlander, P.; Halas, N.J. *Nano Lett.* **2015**, 15, 1272-1280.

[14] Naik, G. V.; Shalaev, V. M.; Boltasseva, A. *Adv. Mater.* **2013**, 25, 3264-3294.

[15] Caldwell, J. D.; Lindsay, L.; Giannini, V.; Vurgaftman, I.; Reinecke, Th. L.; Maier, S. A.; Glembocki, O. J. *Nanophotonics* **2015**, 4, 44-68.

[16] Law, S.; Podolskiy, V.; Wasserman, D. *Nanophotonics* **2013**, 2, 103-130.

[17] Law, S.; Yu, L.; Rosenberg, A.; Wasserman, D. *Nano Lett.* **2013**, 13, 4569-4574.

[18] Wang, T.; Nguyen, V. H.; Buchenauer, A.; Schnakenberg, U.; Taubner, Th. *Opt. Exp.* **2013**, 21, 9005-9010.

[19] N'Tsame Guilengui, V.; Cerutti, L.; Rodriguez, J.-B.; Tournié, E.; Taliercio, T. *Appl. Phys. Lett.* **2012**, 101, 161113.

[20] Ginn, J. C.; Jarecky Jr., R. L.; Shaner, E. A.; Davids, P. S. *J. Appl. Phys.* **2011**, 110, 043110.

[21] Shahzad, M.; Medhi, G.; Peale, R. E.; Buchwald, W. R.; Cleary, J. W.; Soref, R.; Boreman, G. D.; Edwards, O. *J. Appl. Phys.* **2011**, 110, 123105.

[22] Law, S.; Adams, D. C.; Taylor, A. M.; Wasserman, D. *Opt. Exp.* **20**, 12155-12165.

[23] Hoffman, A. J.; Alekseyev, L.; Howard, S. S.; Franz, K. J.; Wasserman, D.; Podolskiy, V. A.; Narimanov, E. E.; Sivco, D. L.; Gmachl, C. *Nature Mater.* **2007**, 6, 946-950.

[24] Soref, R.; Hendrickson, J.; Cleary, J. W. *Opt. Exp.* **2012**, 20, 3814-3824.

[25] Biagioni, P.; Frigerio, J.; Samarelli, A.; Gallacher, K.; Baldassarre, L.; Sakat, E.; Calandrini, E.; Millar, R. W.; Giliberti, V.; Isella, G.; Paul, D. J.; Ortolani, M. *J Nanophot.* **2015**, 9, 093789.

[26] Schwarz, B.; Reininger, P.; Ristanić, D.; Detz, H.; Andrews, A. M.; Schrenk, W.; Strasser, G. Nature Comm. 2014, 5, 4085-4091.

[27] Palubiak, D.P.; Deen, M.J. *IEEE J. Select Topics Quant. Elec.* **2014**, 20, 6000718.

[28] Paul, D. J. *Elec. Lett.* **2009**, 45, 582-584.

[29] Soref, R. *Silicon* **2010**, 2, 1-6.

[30] Soref, R. *Nature Photon.* **2010**, 4, 495-497.

[31] Warburton, R. E.; Intermite, G.; Myronov, M.; Alfred, P.; Leadley, D. R.; Gallacher, K.; Paul, D. J.; Pilgrim, N. K.; Lever, L. J. M.; Ikonic, Z.; Kelsall, R. W.; Huante-Ceron, E.; Knigts, A. P.; Buller, G. S. *IEEE Trans. Elec. Dev.* **2013**, 60, 3807-3813.

[32] Rouifed, M. S.; Chaisakul, P.; Marris-Morini, D.; Frigerio, J.; Isella, G.; Chrastina, D.; Edmond, S.; Le Roux, X.; Coudevylle, J.-R.; Vivien, L. *Opt. Lett.* **2012**, 37, 3960-3962.

[33] Dumas, D. C. S.; Gallacher, K.; Rhead, S.; Myronov, M.; Leadley, D. R.; Paul, D. J. *Opt. Exp.* **2014**, 22, 19284-19292.

[34] Jifeng L.; Sun. X.; Camacho-Aguilera, R.; Kimerling, L. C.; Michel, J. *Opt. Lett.* **2014**, 35, 679-681.

[35] Camacho-Aguilera, R. E.; Cai, Y.; Patel, N.; Bessette, J. T.; Romagnoli, M.; Kimerling, L. C.; Michel, J. *Opt. Express* **2012**, 20, 11316-11320.

[36] Matmon, G.; Paul, D. J.; Lever, L.; Califano, M.; Ikonić, Z.; Kelsall, R. W.; Zhang, J.; Chrastina, D.; Isella, G.; von Känel, H.; Müller, E.; Neels, A. *J. Appl. Phys.* **2010**, 107, 053109.

[37] Chaisakul, P.; Marris-Morini, D.; Frigerio, J.; Chrastina, D.; Rouifed, M.-S.; Cecchi, S.; Crozat, P.; Isella, G.; Vivien, L. *Nat. Photon.* **2014**, 8, 482-488.

[38] Malik, A.; Dwivedi, S.; Van Landschoot, L.; Muneeb, M.; Shimura, Y.; Lepage, G.; Van Campenhout, J.; Vanherle, W.; Van Opstal, T.; Loo, R.; Roelkens, K. *Opt. Expr.* **2014**, 22, 28479-28488.

[39] Chang, Y.-C.; Paeder, V.; Hvozdara, L.; Hartmann, J.-M.; Herzig, H. P. *Opt. Lett.* **2012**, 37, 2883-2885.

[40] TYDEX® materials and coatings database. www.tydexoptics.com/materials1/for_transmission_optics/silicon (accessed August 13, 2015).

[41] Isella, G.; Chrastina, D.; Rössner, B.; Hackbarth, T.; Herzog, H.-J.; König, U.; von Känel, H. *Solid State Electron.* **2004**, 48, 1317.

[42] Rosenblad, C.; Deller, H. R.; Dommann, A.; Meyer, T.; Schroeter, P.; von Känel, H. *J. Vac. Sci. Technol. A* **1998**, 16, 2785-2780.

[43] Zuloaga, J.; Nordlander, P. *Nano Lett.* **2011**, 11, 1280-1283.

[44] Biagioni, P.; Huang, J.-S.; Hecht, B. *Rep. Prog. Phys.* **2012**, 75, 024402.

[45] Giannini, V.; Francescato, Y.; Amrania, H.; Phillips, Ch. C.; Maier, S. A. *Nano Lett.* **2011**, 11, 2835-2840.

[46] Svedendahl, M.; Käll, M. *ACS Nano* **2012**, 6, 7533-7539.

[47] Luk'yanchuk B.; Zheludev, N. I.; Maier, S. A.; Halas, N. J.; Nordlander, P.; Giessen, H.; Chong, C. T. *Nature Mater.* **2010**, 9, 707-715.

[48] Alonso-González, P.; Albella, P.; Schnell, M.; Chen. ,J.; Huth, F.; García Etxarri, A.; Casanova, F.; Golmar, F.; Arzubiaga, L.; Hueso, L. E.; Aizpurua, J.; Hillenbrand, R. *Nature Comm.* **2012**, 3, 684-690.

[49] Vanhellemont, J.; Simoen, E. *Mater. Sci. Semicond. Proc.* **2012**, 15, 642-655.

[50] Klesse, W. M.; Scappucci, G.; Cappellini, G.; Hartmann, J. M.; Simmons, M. Y. *Appl. Phys. Lett.* **2013**, 102, 151103.

Table of Contents Graphic

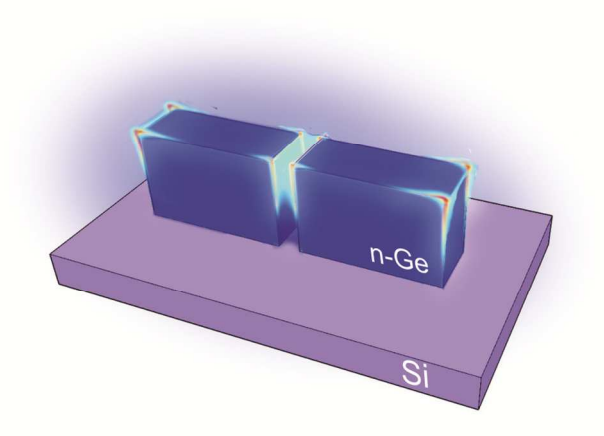

Mid-infrared plasmon-enhanced spectroscopy with germanium antennas on silicon substrates

Leonetta Baldassarre[1,2], Emilie Sakat[3], Jacopo Frigerio[4], Antonio Samarelli[5], Kevin Gallacher[5], Eugenio Calandrini[1], Giovanni Isella[4], Douglas J. Paul[5], Michele Ortolani[1], Paolo Biagioni[3]

[1]*Dipartimento di Fisica, Università di Roma "La Sapienza", Piazzale Aldo Moro 5, I-00185 Roma, IT*

[2]*Center for Life Nano Science@Sapienza, Istituto Italiano di Tecnologia, Viale Regina Elena 291, I-00161 Roma, IT*

[3]*Dipartimento di Fisica, Politecnico di Milano, Piazza Leonardo da Vinci 32, I-20133 Milano, IT*

[4]*LNESS, Dipartimento di Fisica del Politecnico di Milano, polo di Como, via Anzani 42, I-22100 Como, IT*

[5]*School of Engineering, University of Glasgow, Rankine Building, Oakfield Avenue, Glasgow G12 8LT, UK*

Corresponding author's email address: paolo.biagioni@polimi.it

SUPPORTING INFORMATION

A. Methods

Ge growth

The Ge epitaxial material was grown by low energy plasma enhanced chemical vapour deposition (LEPECVD) [S1, S2]. This growth technique is a variant of the conventional chemical vapour deposition characterized by the use of a low energy plasma to control the deposition of silicon-germanium alloys. The plasma is able to strongly enhance the deposition efficiency if compared to conventional chemical vapour deposition and the low energy of ions (≈ 10 eV) avoids damage of the substrate and allows the deposition of crystalline materials. In a LEPECVD reactor, a tantalum filament inside the plasma source is heated by a high current (130 A), so that electrons are thermionically emitted. Argon gas is passed up through the plasma source into the growth chamber. A direct current arc discharge of 30-50 A with a low voltage of 30 V can then be sustained between the filament and the growth chamber; an anode ring is mounted within the growth chamber to stabilize the discharge. Magnetic fields (created by coils) are used to focus the plasma onto the substrate, which is heated from behind by a graphite heater. Precursors gases (GeH_4 for germanium, PH_3 for doping) are introduced in the chamber, where the highly-reactive conditions created by the plasma cause the material to be efficiently deposited on the substrate. This gives great flexibility in the growth of high quality material, since the growth rate, controlled by the plasma density and by the amount of process gas, and the mobility of the adatoms, controlled by the substrate temperature, can be optimized separately. The sample was grown on a 100 mm p-Si(001) substrate with a resistivity of 5-10 Ohm·cm.

Before the heteroepitaxy, the native oxide was removed by dipping the substrate in aqueous hydrofluoric acid solution (HF :H_2O 1:10) for 30 s. A 1 μm n-doped ($n \approx 2.5 \times 10^{19}$ cm^{-3}) Ge layer was deposited at 500 °C at a growth rate of 1 nm/s, with a GeH_4 flow of 20 sccm. The n-type doping was achieved in-situ by adding 0.15 sccm of PH_3.

Antenna patterning

Electron beam lithography was undertaken using a Vistec VB6 UHR tool at 100 keV. Hydrogen silsesquioxane (HSQ) resist was spun onto the samples to produce a thickness of 520 nm. After patterning, the HSQ resist was developed using a diluted tetramethyl ammonium hydroxide (TMAH) based solution with dionised water of 1:4 concentration for 30 s at 23 ˚C. The samples were then etched in a STS Multiplex silicon etcher inductively coupled plasma (ICP) reactive ion etch system using SF_6 and C_4F_8 gases in a mixed process [S3] using a laser end-point detection system to stop the process once etching through the Ge epilayer had been completed. Finally the resist was removed using HF.

Electromagnetic simulations

Frequency-domain simulations have been performed with the free software "Reticolo" [S4], employing the rigorous coupled-wave analysis (RCWA), and with the finite-difference time domain method [S5].

Infrared spectroscopy

Infrared measurements were carried out with a Fourier transform infrared (FTIR) spectrometer from Bruker (IFS66v), operated in vacuum to eliminate infrared absorption lines due to the atmosphere. Measurements were performed with a broadband globar source and using a 77 K HgCdTe photovoltaic detector and a 4.2 K Si bolometer for low-noise cryogenic detection of mid- and far-IR radiation, respectively. Two optical schemes were used: direct transmission and specular reflection. For the transmission measurements, the samples were mounted on a vacuum manipulator inserted in the sample compartment of the FTIR. A 4x4 mm^2 portion of the same Ge-on-Si wafer was used as the reference where the antennas were etched off leaving the blank silicon wafer. A displaceable circular metal frame with a hole diameter of 4 mm was used to select the portion of the chip were the antenna arrays were located. The absolute reflectivity of the antenna arrays was measured at several incidence angles including near-normal incidence with a home-built setup based on off-axis parabolic and plane mirrors, with a spot size of about 3 mm, smaller than the 5x5 mm^2 area occupied by the antenna array, thus allowing for easy and precise alignment. On the same sample holder a co-aligned gold mirror was then mounted close to the sample position and used as a reference.

PDMS experiments

The fabricated structures were spin-coated with PDMS starting from a 100:1 (v/v) mixture of monomer and curing agent, diluted in a 5% (v/v) solution in n-heptane, in order to lower the viscosity and facilitate thin homgeneous layer formation. After spin-coating, the mixture was then left undisturbed for 2 hours to allow the solution to smoothly cover the steep walls and edges of the antenna structures, and moreover to penetrate into the double arm antenna gap. The mixture was then cured for 30 minutes

at 80 °C in order to allow for elastomer reticulation hence forming the continuous PDMS film coating all antennas on the chip with almost perfect adhesion. The only point where adhesion was not successful is the bottom part of the double-arm antenna gaps (see Fig. 3a and discussion in the main text).

AZ5214 experiments

The Novolac-resin AZ5214 polymer was purchased from Clariant GmbH, diluted 1:50, spin-coated at 5000 rpm, and finally baked on a hot plate at 90 °C for 60 s.

CEMS experiments

CEMS was purchased from Sigma-Aldrich and the liquid was used in its pure form. It was drop-casted on the antenna chip by an Eppendorf micropipette inside the FTIR setup.

B. Dielectric constant extraction of the unpatterned Ge material

Spectroscopic measurements of the infrared (IR) reflectance at near-normal incidence $R(\omega)$ and of the transmittance $T(\omega)$ for radiation frequency ω between 50 and 5000 cm^{-1} were performed on n-doped germanium-on-silicon (n-Ge-on-Si) wafer portions with different doping levels to fully characterize the as-grown material. The room-temperature data demonstrated in Fig. S1a are relative to the sample that was used for the fabrication of the plasmonic antenna arrays. For this sample, an estimated free carrier density $n_e \approx 2.1\ 10^{19}$ cm^{-3} is obtained from a measured plasma frequency $\omega_p \approx 974$ cm^{-1} using the formula reported in the article text and, more extensively, in Ref. S1. Here ω_p is defined as the frequency of zero-crossing of the real part of the dielectric function $\varepsilon_1(\omega)$, which was in turn calculated from the Drude model with parameters obtained from a best fit of the far-IR $R(\omega)$ spectrum alone (see below). The carrier densities estimated in this way are in good agreement with those provided by DC transport data on Hall bar devices [S6]. A more precise knowledge of the carrier density and more generally of the complex dielectric function beyond the simplistic Drude model, however, is required to perform accurate electromagnetic simulations. Below we provide details on how all these key physical quantities were determined from the spectroscopic data taken on the unpatterned Ge film before the fabrication of the antennas.

For $\omega < \omega_p$, $R(\omega)$ has a high absolute value close to 1. In this far-IR region, the skin depth is below 1 μm, smaller than the n-Ge film thickness. Therefore, the normal-incidence transmittance T was found to be negligibly small, and we can assume that the nGe film behaves as a semi-infinite medium. This implies that the two-variable system of equations relating $R(\omega)$ and $T(\omega)$ to the real and imaginary parts of the dielectric function $\varepsilon_1(\omega)$ and $\varepsilon_2(\omega)$ cannot be used in this case, and we have to find a different method to determine the dielectric function. For $\omega > \omega_p$, nGe behaves as a dielectric material, since $\varepsilon_1 > 0$. The sinusoidal-like oscillations observed in both $R(\omega)$ and $T(\omega)$ above 1000 cm^{-1} are due

to multiple internal reflection interference within the n-Ge layer (Fabry-Perot fringes). The specific shape of the fringe pattern is due to the dielectric function of n-Ge being strongly frequency-dependent. By employing a more complex fitting procedure that combines the multilayer Fresnel relations and the Drude-Lorentz model, it was possible to satisfactorily reproduce the $R(\omega)$ data in the whole IR range up to 5000 cm^{-1} and hence to obtain a better estimate of the activated carrier density $n_e \approx 2.32\ 10^{19}\ cm^{-3}$. In this case, n_e was not determined from ω_p (defined as the zero-crossing of ε_1) but rather from the so-called Drude spectral weight, i.e. the intensity of the zero-frequency oscillator in the optical conductivity usually referred to as the 'Drude term'. As stated above, the $R(\omega)$ data are fairly well reproduced by the curve fitting based on the Drude-Lorentz model, with the exception of a small frequency range just below ω_p ($900 < \omega < 974\ cm^{-1}$), where the n-Ge still displays metallic behaviour but a significant fraction of the radiation is transmitted through the n-Ge due to the skin depth becoming larger than the film thickness. This is a very relevant issue, because the knowledge of the exact values of $\varepsilon_1(\omega)$ and $\varepsilon_2(\omega)$ beyond the simple Drude model is crucial for the accurate modelling and simulation of the plasmonic antennas and devices. Indeed, the Drude model provides reasonable values of n_e since this corresponds to the spectral weight of the Drude term, which is an integral quantity determined from the data taken over the entire IR range, but the functional form of the Drude term is known to inadequately describe the frequency-dependent electron-lattice scattering processes that determine the exact shape of the dielectric function in the vicinity of ω_p [S7]. We now briefly describe the method employed to retrieve the dielectric function (more details can be found in Ref. S8).

The above mentioned initial fitting procedure based on the Fresnel relations and the Drude model allowed us to retrieve an analytical approximation of the dielectric constant of n-Ge. We used this analytical model to compute the absolute reflectance $R(\omega)$ of a virtual semi-infinte n-Ge material in the non-zero transmittance region just below ω_p and also in the dielectric region $\omega > \omega_p$. For the high-reflectivity region $\omega < \omega_p$ we took the raw experimental data collected on the n-Ge film, merged with the result of the above computation. We finally obtain an extrapolation of the experimental $R(\omega)$ towards zero frequency and infinity. At this point, we resort to the model-independent approach based on Kramers-Kronig transformations applied to the prolonged $R(\omega)$. Through the Kramers-Kronig integral applied to $\ln[R(\omega)]$ we calculated the phase of the complex reflectance coefficient $\theta(\omega)$ and then, from both functions, the real and imaginary part of the dielectric constant, as demonstrated in Fig. S1b and S1c.

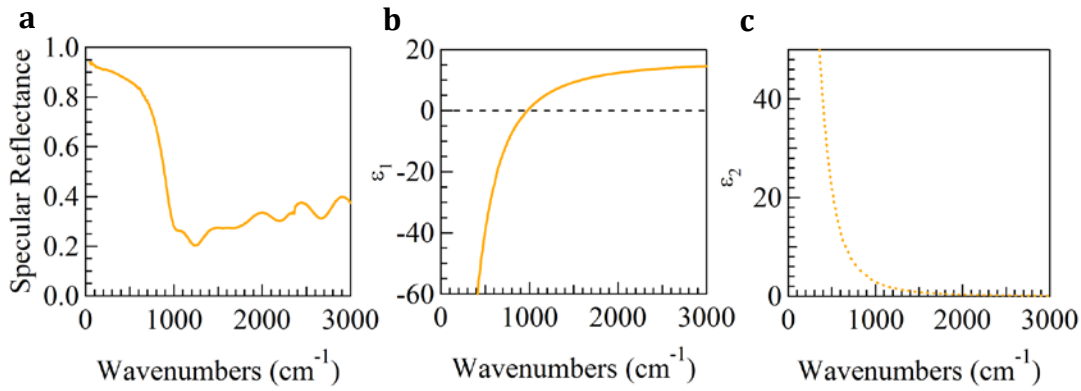

Figure S1 | The reflectance spectrum and extracted dielectric constant of the Ge material. **a,** The reflectivity curve measured on the unpatterned nGe-on-Si sample wafer before the fabrication process. **b-c,** The real (**b**) and imaginary (**c**) parts of the dielectric constant as obtained by the Kramers-Kronig transformations of the extrapolated $R(\omega)$ curve (see text for details).

C. Electromagnetic simulations

In order to understand and design the antenna response, we ran extensive electromagnetic simulations, as described in Section A. Fig. S2 demonstrates a representative example of the simulated transmission spectra at normal incidence as a function of the antenna length with the electric field polarization parallel to the long antenna axis, demonstrating the two R1 and R2 resonances that are widely discussed in the main text. As expected, the two resonances demonstrate a clear red-shift for increasing antenna length. The vertical, non-dispersing discontinuity that can be observed around 590 cm^{-1} for all antenna lengths is due to the appearance of a diffracted order, generating a so-called Rayleigh anomaly that does not strictly superimpose with the R1 resonance for the antenna lengths that have been investigated experimentally. Rayleigh anomalies and the presence of diffracted orders will be addressed in Section E of the Supplementary Information. For the sake of completeness, it should be noted that some of the Rayleigh anomalies enter the $\omega < 1000$ cm^{-1} region because of the specific periodicity of the array. In general, they leave very weak imprints in the extinction spectra, that can be recognized as slight changes of slope e.g. around 590 cm^{-1} in Fig 2c and around 405 cm^{-1} in Fig. 2d in the main article text. In the only case where one Rayleigh anomaly is found very close to the extinction peak of the substrate-like resonance R1 (i.e. the peak around 420 cm^{-1} of the $L = 3$ μm antenna in Fig. 2e), a clearer discontinuity is observed in the peak profile. All other plasmon resonance peaks discussed in the main manuscript, and in particular all the R2 resonances employed for molecular sensing, are completely free from the influence of Rayleigh anomalies.

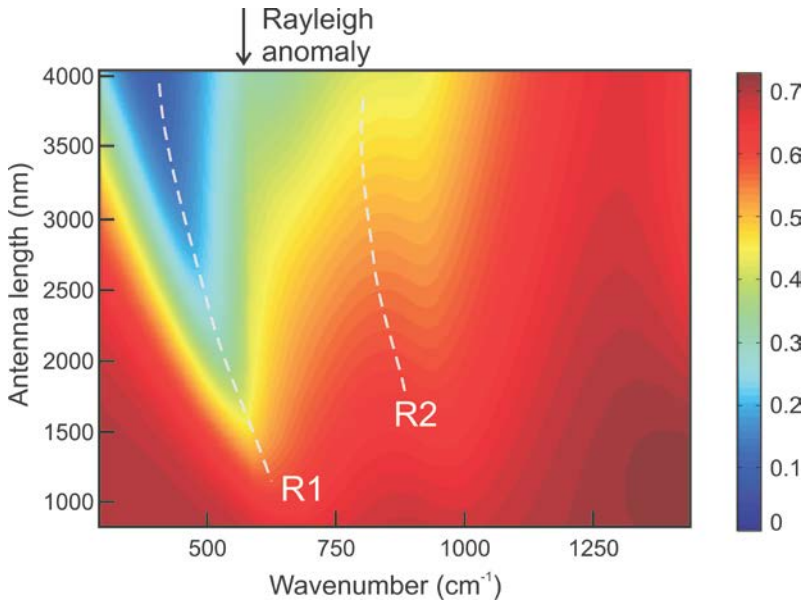

Figure S2 | The simulated transmission spectra for varying antenna length. The simulated transmission spectra as a function of the antenna length in an array of single-arm antennas after plane-wave excitation with electric field polarization parallel to the antenna axis.

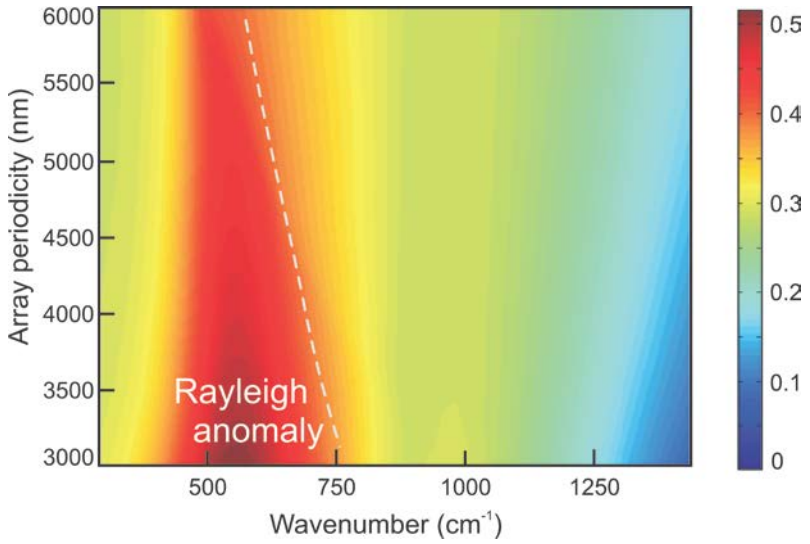

Figure S3 | The simulated reflection spectra for varying periodicity of the array. The simulated reflection spectra as a function of the periodicity of the array in an array of single-arm antennas with $L = 2$ μm after plane-wave excitation with electric field polarization parallel to the antenna axis.

As a further proof that the designed R1 and R2 resonances are due to localized current oscillations in the plasmonic antennas and not to grating-related effects, we also ran simulations for a $L = 2$ μm

antenna varying the periodicity of the array along the direction parallel to the main antenna axis. Results in Fig. S3 demonstrate that the two resonances do not shift with the periodicity, while the only dispersing feature (dashed line) is again related to a Rayleigh anomaly, which comes close to the R1 resonance only for periodicities much larger than the one investigated experimentally for the L = 2 μm antenna sample.

Finally, it should be noted that the lossy nature of plasmonic Ge produces a red-shift of the resonance in the near-field intensity compared to the far-field resonances observed in far-field extinction spectra, as is well documented in the literature and reported in Fig. S4, where we demonstrate the comparison between simulated extinction and near-field intensity spectra for gap antennas with 2 μm arm length.

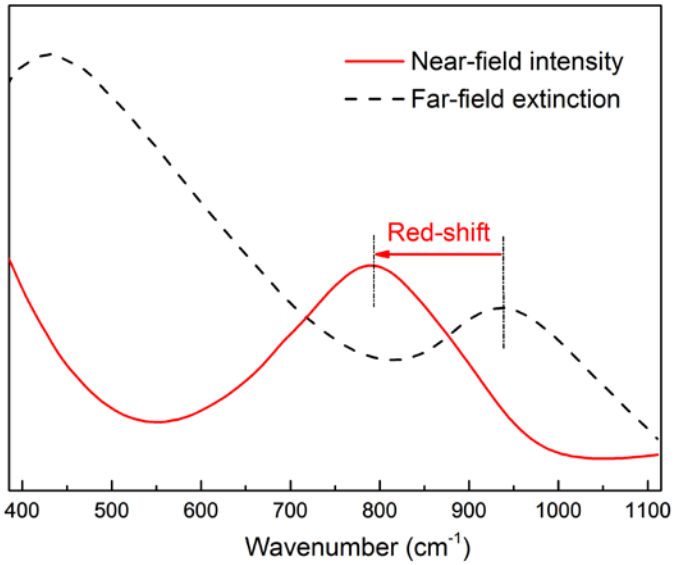

Figure S4 | The simulated extinction and near-field intensity spectra of a gap antenna. The simulation for a gap antenna with arm length L = 2 μm reveals the red-shift of the near-field resonances compared to the spectral position of the far-field extinction peaks.

D. Geometrical details of the samples investigated in the main manuscript

Sample	*L* (μm)	*W* (μm)	*dx* (μm)	*dy* (μm)	g (μm)
1 (Fig. 2c)	2	0.8	5	2	-
2 (Fig. 2d)	2	0.8	7.3	2	0.3
3 (Fig. 2e)	3	0.8	7	2	-

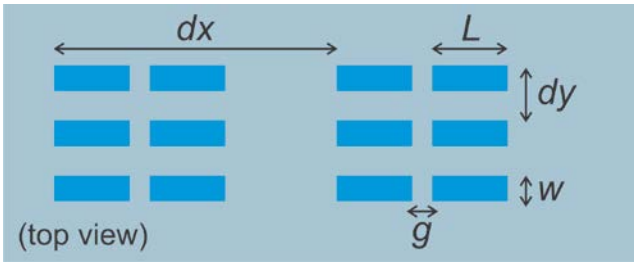

Figure S5 | The geometry of the investigated samples. A sketch of the geometry of the samples discussed in the main text. In the table, samples are numbered from 1 to 3 and a reference to the related figures in the main text is added.

E. Detailed analysis of the infrared spectra of the antenna arrays

The two resonances R1 and R2 discussed in the article text are attributed to two distinct resonant modes propagating along the antenna long axis. This assignment is based on a full body of simulations (see also Section C of the Supplementary Information) and infrared reflectance measurements that we performed as a function of the incidence angle, with electric field polarization direction both parallel and perpendicular to the antenna axis and, for each of the two sample orientations, also with the electric field vector contained in the incidence plane or perpendicular to it. All infrared measurements were identically repeated on copies of the arrays, fabricated on a different Ge-on-Si wafer, where the doping level was of the order of 10^{17} cm^{-3}. This material is referred to as 'undoped' throughout this work since the charge density, although relevant for determining the DC conduction properties, is too small to give imprints in the infrared range. The combined analysis of all the acquired spectra allowed us to unambiguously conclude that: (i) the R1 and R2 resonances do not appear in the undoped material; (ii) the R1 and R2 peaks described as plasmonic resonances in the article text are present only when the polarization of the electric field vector is directed along the antenna arm; (iii) R1 and R2 are not due to Bragg-like modes of the periodic array structure. Here we complement this information by presenting and discussing some selected features of the infrared transmission and reflection spectra.

First of all, it should be noted that, as is well-known from the theory of plasmonic antennas, transverse resonances should be expected as well in our samples. Indeed Fig. S6 compares experiments and simulations obtained with electric field polarization parallel or perpendicular to the antenna axis for a double-arm gap antenna. Two broad and weak features centered at about 600 and 900 cm^{-1}, which can be more easily recognized in the simulated spectra, appear for the perpendicular polarization (dashed lines) and can be attributed to resonant transverse oscillations of the conduction electrons. The net dipole moment induced by such resonances, however, is weaker than the one for the longitudinal resonances, which results in an accordingly weaker (sometimes negligible) far-field spectral signature. As expected, transverse antenna resonances are blue-shifted compared to the respective longitudinal resonances.

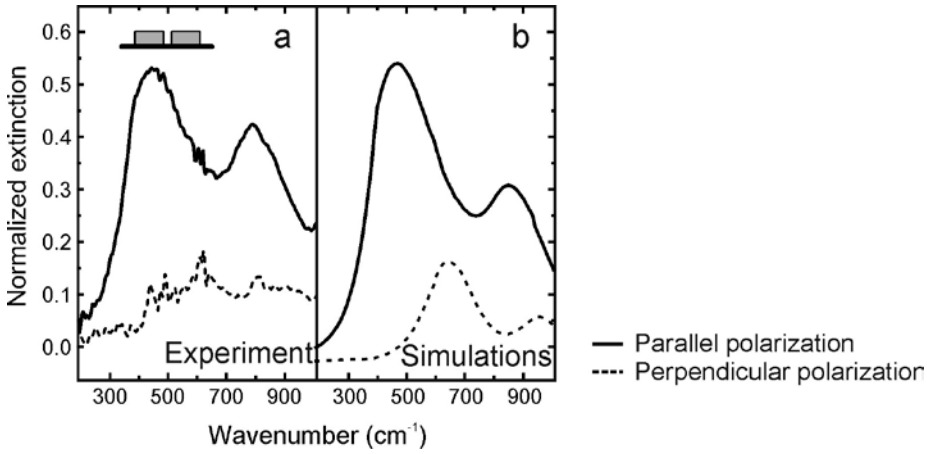

Figure S6 | The experimental and simulated normalised extinction spectra for different electric field polarizations. a, The experimental extinction spectra for electric field polarization parallel (solid line) and perpendicular (dashed line) to the antenna axis. **b,** The simulated extinction spectra for electric field polarization parallel (solid line) and perpendicular (dashed line) to the antenna axis.

Fig. S7 presents further selected experimental results, demonstrating the same weak transverse resonances for both gapless and gap antennas and also confirming that for both electric field polarization parallel and perpendicular to the antenna axis the response of an undoped sample with the same nominal geometry is flat within the experimental noise.

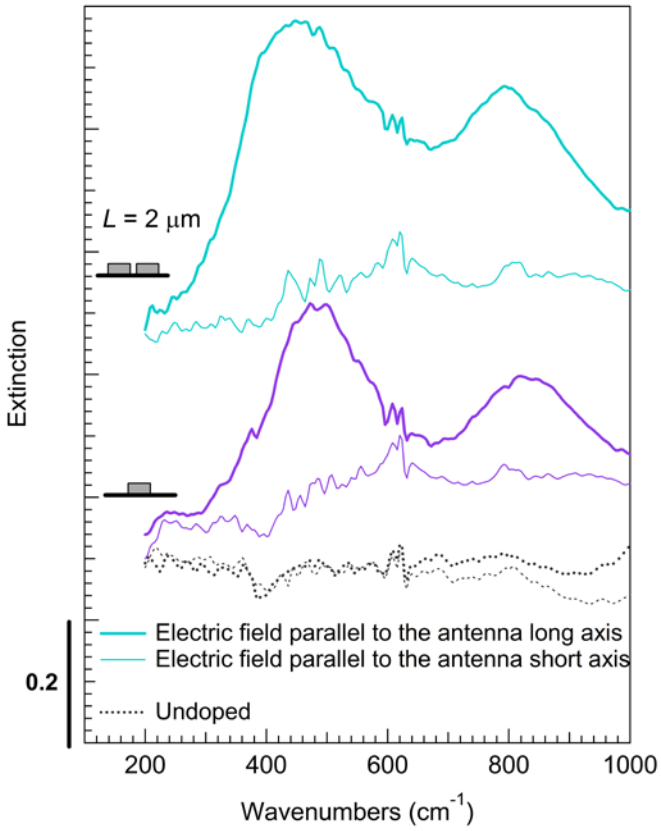

Figure S7 | The experimental extinction spectra for different antennas and different electric field polarizations. The extinction spectra with parallel (thick lines) and perpendicular (thin lines) polarization of the L = 2 μm antenna arrays (both gapless and gap antennas, see sketches). The dotted lines refer to an undoped sample. The set of data for the double-arm gap antenna has been vertically shifted for clarity.

The sharp increased-noise feature at 610 cm^{-1}, visible in all spectra and for both orientations of the electric field, is an artifact due to the Raman-active phonon of the Si substrate that oscillates exactly at that frequency. The Raman-active phonon becomes weakly IR active in virtually all commercial Si wafers due to the presence of symmetry-breaking impurities. As a consequence, the signal-to-noise ratio of infrared spectra taken on samples with Si substrates usually drops around 610 cm^{-1}, because it is not possible to fully compensate for the rapidly-varying optical constants of the Si substrate in both the sample spectra and the bare Si spectral reference.

To confirm that the spectra from doped and undoped antennas differ only in the presence of the localized plasmon resonances, we demonstrate in Fig. S8 a representative example with specular reflectance spectra taken at near-normal incidence from the L = 2 μm single-arm antenna array. These results confirm that all the spectral features above 1000 cm^{-1} are present both in the doped and undoped antenna sample, although with small differences due to slight changes in the Ge refractive index because of doping, while the spectral region below 1000 cm^{-1} demonstrates clear differences in the

two samples because of the appearance of the R1 and R2 resonances discussed in the main text (see left panel). A weak signature of the transverse plasmon resonance is also visible around 900 cm^{-1} in the undoped sample for the perpendicular polarization (see right panel).

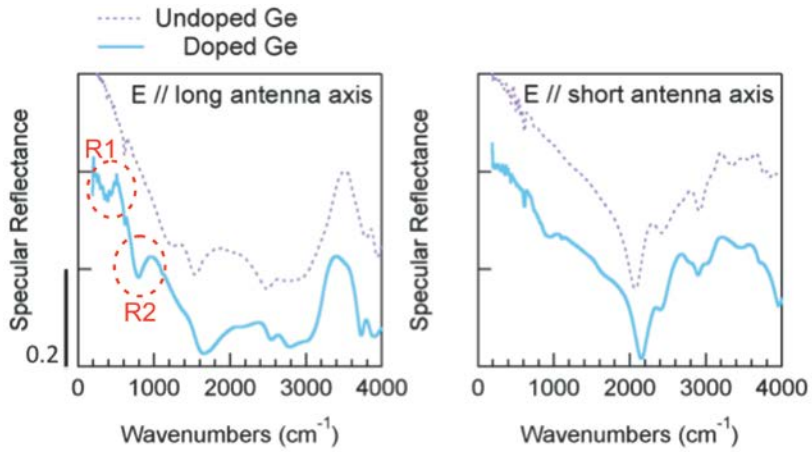

Figure S8 | The experimental reflectance spectra. The specular reflectance measured at near-normal incidence with electric field polarization parallel to the long (left panel) and short (right panel) antenna axis for the L = 2 μm single-arm antenna array. The antennas fabricated out of both doped (solid line) and undoped (dashed line) material have been measured, with their respective spectra being virtually identical with the sole exception of the appearance of the signature related to the R1 and R2 resonances (dashed circles in the left panel).

Since we fabricated extended antenna arrays in order to be able to perform far-field spectroscopic experiments in the full IR range with almost-collimated beams, grating modes appear in the transmission and reflection spectra as Rayleigh anomalies (abrupt variations of both reflectance and transmittance at a given frequency). We performed an extensive study of the Rayleigh anomalies in order to exclude any contribution of these modes arising from Bragg diffraction in the arrays to the observed plasmonic resonances. We measured both specular and non-specular angle-resolved reflectance spectra in the mid-IR region (500 to 3000 cm^{-1}) to identify all possible resonant optical features of the antenna arrays, using an optical setup with illumination and collection angles that can be separately varied. The setup is comprised of two spherical mirrors, collecting light on a cone with apical half-angle of 6°, that can be remotely controlled in vacuum so as to vary the elevation angle between 0° and 90° (a sketch of the optical setup is reported in Fig. S9a). The specular reflectance spectra of the single antenna arrays with L = 3 μm for several incidence/collection angles are reported in Fig. S9b. When the incidence light is polarized parallel to the antenna axis and the electric-field vector is contained in the incidence plane (so called 'p' polarization), the specular reflectance displays a smooth decrease with increasing frequency, reminiscent of the normal-incidence reflection spectra

of the unpatterned sample (see Fig. S1), plus a peak around 800-900 cm^{-1} and a feature around 1600-2000 cm^{-1} dispersing to higher energies for increasing incidence angle. The former series of peaks can be attributed to the R2 antenna resonance and does not show any significant dependence of the peak frequency on the incidence angle, as expected for localized plasmon resonances. At variance, the latter series of peaks clearly blue-shifts with increasing incidence/collection angle. In the non-specular reflectance configuration (Fig. S9c) the zero-order reflected intensity is eliminated and the plasmonic resonance around 800-900 cm^{-1} disappears from the spectra, while grating modes remain clearly visible, and are peaked at different wavelengths for different collection angles θ, following the Bragg's law for a normally-incident plane wave:

$$\omega_{\text{Bragg}}(i,j,\theta) = \sqrt{\left(\frac{i}{a\ \sin\theta}\right)^2 + \left(\frac{j}{b}\right)^2}$$

where a and i are the periodicity and the mode order in the direction parallel to the antenna axis, while b and j refer to the direction perpendicular to the antenna axis in the sample plane.

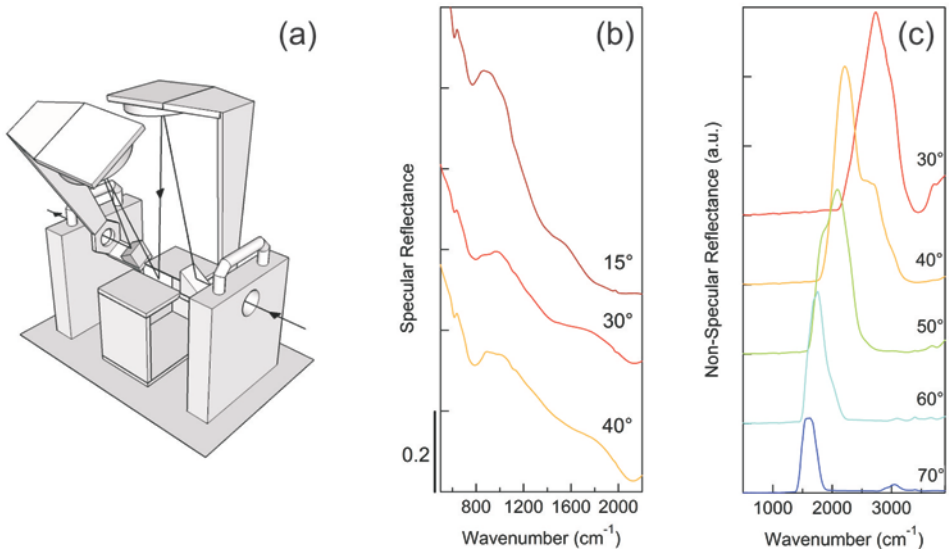

Figure S9 | The angle-resolved reflectance spectra. a. A sketch of the optical setup used for specular and non-specular reflectance measurements. **b.** The specular reflectance for different incidence/collection angle from the L = 3 μm single-arm antenna array. **c.** The non-specular reflection at normal incidence for several non-normal collection angles.

F. Absorbance spectra of PDMS and CEMS

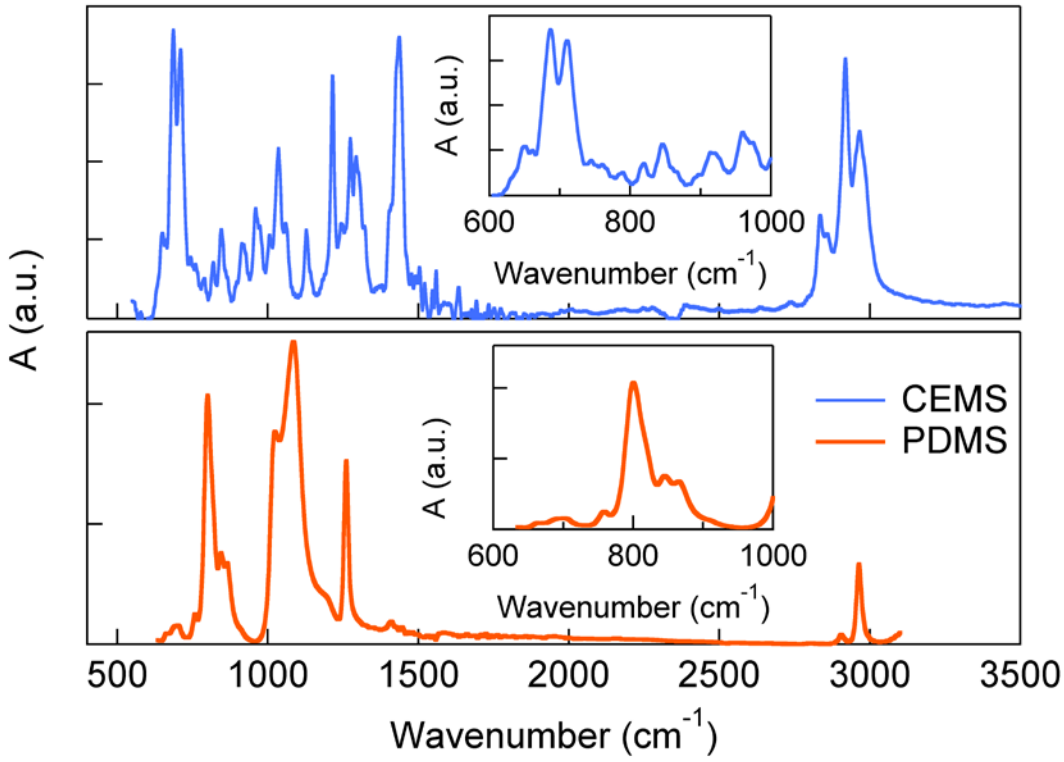

Figure S10 | The absorbance spectra of PDMS and CEMS. The absorbance A of the substances used for sensing in the two experiments described in the main text. The absorbance was determined from FTIR transmission measurements on solid (PDMS) or liquid (CEMS) films prepared in the same way as those used for sensing, although with a much larger thickness to increase the FTIR signal-to-noise ratio. The inset shows the spectral region of interest for the localized plasmon resonances of the investigated Ge antennas.

G. PDMS sensing: comparison with a weakly-absorbing polymer

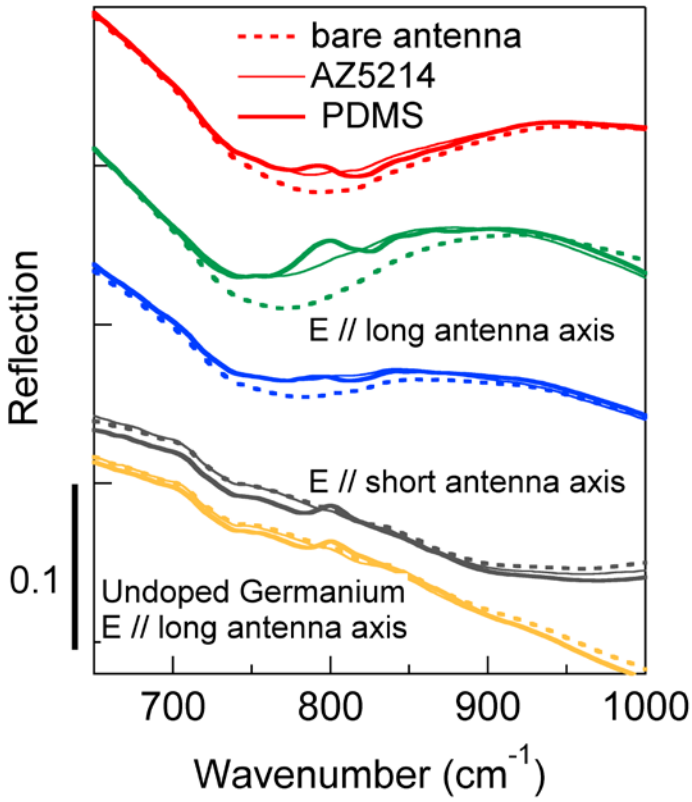

Figure S11 | Line shape extraction for antenna-enhanced PDMS sensing. We demonstrate the reflection spectra for PDMS-coated (thick solid lines) and AZ5214-coated (thin solid lines) antennas. Doped antennas are represented red, green, and blue; undoped antennas are represented yellow; the black line is a representative example from doped antennas studied with polarization perpendicular to the antenna axis.

H. PDMS sensing: comparison with undoped antennas

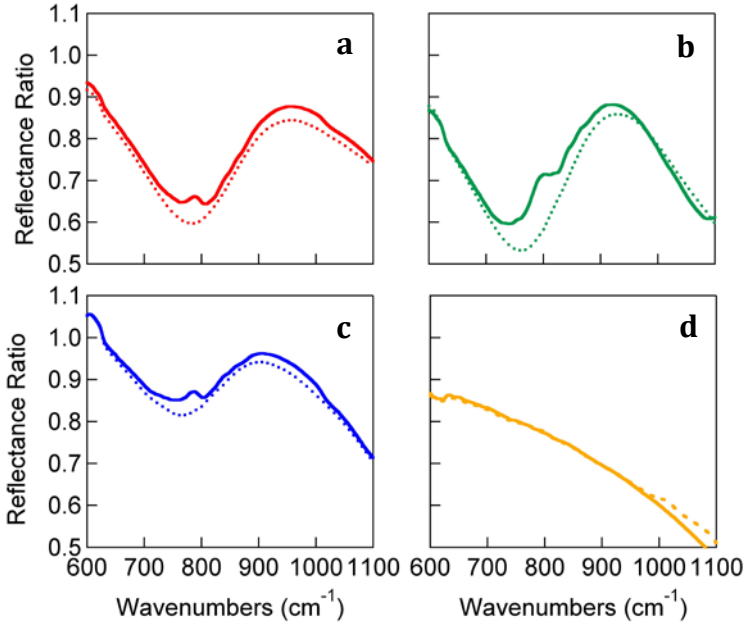

Figure S12 | The normalized spectra for antenna-enhanced PDMS sensing. We calculate the ratio between the spectra obtained for parallel and perpendicular light polarization from clean antennas (dashed lines) and PDMS-coated antennas (solid lines). While PDMS-coated plasmonic antennas (red, blu, and green lines, panels a-c) maintain the vibrational feature at 800 cm^{-1} after normalization, the latter completely disappears in the case of nominally undoped antennas (yellow line, panel d), clearly highlighting the coupling between the vibrational resonances and the longitudinal plasmonic resonances.

I. PDMS sensing: role of the R1 resonance

In order to exclude any influence from the tails of the R1 localized resonance on the PDMS feature around 800 cm^{-1}, we performed FDTD simulations with the exact same materials and templates as in Fig. 4 but with the PDMS only in the position of the R1 hot spots. The results, demonstrated in the figure below, show no trace of the PDMS vibrational feature and therefore confirm that R1 plays no role in the observed line shapes.

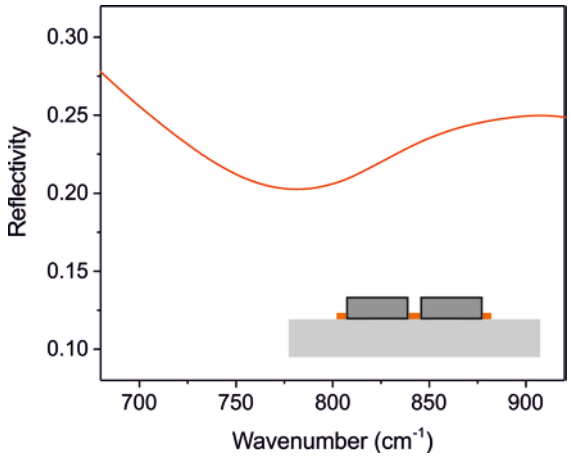

Figure S13 | Sensing simulations with the R1 hot spots. We plot the calculated reflectivity obtained from FDTD simulations for a gap antenna with the PDMS placed at the position of the R1 hot spots.

J. CEMS sensing: simulated near-field enhancement

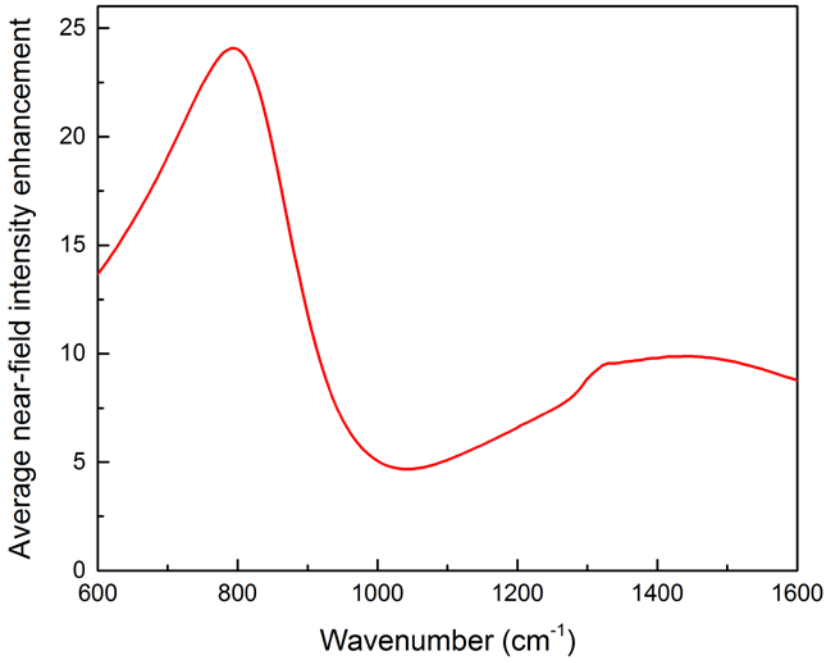

Figure S14 | The average near-field intensity enhancement for the antenna in the CEMS sensing experiment. To qualitatively support the results in Fig. 5 of the main manuscript, we demonstrate here the simulated near-field intensity enhancement averaged around the antenna at a distance of 50 nm from the surface, clearly highlighting the larger overall enhancement obtained in the plasmonic spectral region below 1000 cm^{-1}.

References

[S1] Isella, G.; Chrastina, D.; Rössner, B.; Hackbarth, T.; Herzog, H.-J.; König, U.; von Känel, H. Solid State Electron. **2004**, 48, 1317-1323.

[S2] Rosenblad, C.; Deller, H. R.; Dommann, A.; Meyer, T.; Schroeter, P.; von Känel, H. J. Vac. Sci. Technol. A **1998**, 16, 2785-2780.

[S3] Mirza, M. M.; Zhou, H.; Velha, Ph.; Li, X.; Docherty, K. E.; Samarelli, A.; Ternent, G.; Paul, D. J. J. Vac. Sci. Technol. B **2012**, 30, 06FF02.

[S4] Hugonin, J. P.; Lalanne, P. Reticolo software for gratig analysis. Institut d'Optique, Orsay, France (2005).

[S5] FDTD Solutions, version 8.5.3; Lumerical Solutions, Inc.: Canada, 2013.

[S6] Ortolani, M.; Baldassarre, L.; Nucara, A.; Samarelli, A.; Paul, D.J.; Frigerio, J.; Isella, G.; Finazzi, M.; Biagioni, P. IEEE Proc. of the 38th International Conference on Infrared, Millimeter, and Terahertz Waves (IRMMW-THz 2013), Mainz, Germany, September 2013.

[S7] Spitzer, W.G.; Fan, H.Y. Phys. Rev. **1956**, 106, 882.

[S8] Baldassarre, L.; Calandrini, E.; Samarelli, A.; Gallacher, K.; Paul, D.J.; Frigerio, J.; Isella, G.; Sakat, E.; Finazzi, M.; Biagioni, P.; Ortolani, M. IEEE Proc. of the 39th International Conference on Infrared, Millimeter, and Terahertz Waves (IRMMW-THz 2014), Tucson (AZ), USA, September 2014